Computational Fluid Dynamics Modeling of Immobilized Photocatalytic Reactors for Water Treatment

J. Esteban Duran, Madjid Mohseni and Fariborz Taghipour
Dept. of Chemical and Biological Engineering, The University of British Columbia, Vancouver, BC V6T 1Z3, Canada

DOI 10.1002/aic.12399
Published online September 29, 2010 in Wiley Online Library (wileyonlinelibrary.com).

A computational fluid dynamics (CFD) model for the simulation of immobilized photocatalytic reactors used for water treatment was developed and evaluated experimentally. The model integrated hydrodynamics, species mass transport, chemical reaction kinetics, and irradiance distribution within the reactor. The experimental evaluation was performed using various configurations of annular reactors and ultraviolet lamp sizes over a wide range of hydrodynamic conditions ($350 < Re < 11{,}000$). The evaluation showed that the developed CFD model was able to successfully predict the photocatalytic degradation rate of a model pollutant in the analyzed reactors. In terms of hydrodynamic models, the results demonstrated that the laminar model performs well for systems under laminar flow conditions, whereas the Abe-Kondoh-Nagano low Reynolds number and the Reynolds stress turbulence models give accurate predictions for photoreactors under transitional or turbulent flow regimes. The performed analysis confirmed that degradation rates of organic contaminants in immobilized photocatalytic reactors are strongly limited by external mass transfer; as a consequence, the degradation prediction capability of the CFD model is largely determined by the external mass transfer prediction performance of the hydrodynamic models used.
 AIChE J, 57: 1860–1872, 2011
Keywords: CFD, immobilized photocatalyst, photocatalysis, water treatment, annular reactor

Introduction

The contamination of drinking water sources with harmful organic substances has been recognized as a major problem worldwide. Among many other compounds, pesticides, pharmaceuticals, and personal care products are now frequently found in water resources and outflows from sewage treatment plants.[1–3] The removal of these contaminants using conventional water treatment processes has shown to be very difficult; therefore, an increasing number of new treatment technologies are being developed and evaluated. A particularly emerging and promising technology is heterogeneous photocatalysis.[4] Photocatalytic processes involve the use of nanostructured photocatalyst materials, predominantly titanium dioxide (TiO_2), activated by ultraviolet (UV) irradiation. One of the main appeals of this technology lies in its capability to potentially mineralize the pollutants into harmless compounds (carbon dioxide, water, and mineral acids) without producing any other waste streams.[5]

Despite the many advantages of photocatalysis and the extensive laboratory research done in this field, there are still some factors that stymie the development of large scale

Correspondence concerning this article should be addressed to F. Taghipour at fariborz@chbe.ubc.ca.

photocatalytic oxidation reactors for water treatment. Lack of proper models and simulation tools for predicting and analyzing the performance of full-scale systems, and therefore lack of adequate scale-up strategies, is among the key factors hindering the development of commercial water treatment systems using this technology.[6–8] An effectual approach to this issue is the application of computational fluid dynamics (CFD), which has extensively demonstrated to be a very effective tool in the design, optimization and scaling up of reacting systems.[9–10] Through simultaneous modeling of hydrodynamics, species mass transport, chemical reaction kinetics, and photon flux distribution, CFD allows for comprehensive analysis of photocatalytic reactor performance by providing the local values of the parameters of interest (i.e., fluid velocity, pollutant concentration, reaction rate, UV irradiance, etc.). In addition, applying CFD analysis to scaled-up reactors minimizes experimental effort and fabrication costs at the pilot-scale level.[7]

Most of the CFD models of photocatalytic reactors reported in the literature are related to the simulation of immobilized photocatalytic reactors used for air treatment.[11–15] There are few CFD investigations of photocatalytic reactors used for water treatment.[16–18] For the case of turbulent flow immobilized photocatalytic reactors for water treatment, to the authors' knowledge, only two investigations are reported in the literature. In one of them,[19–20] a series of simulations were run to determine the effects of flow rates, diffusion coefficients, reaction rate constants, and inter lamp spacing on the performance of a multilamp reactor. One of the main findings of the investigation was that the conversion in the reactor was primarily controlled by the flow and diffusion of the pollutant, and was practically independent of the surface reaction rate. However, the publications neither offer much information about the computational model (boundary conditions, radiation model, near-wall modeling approach, mesh quality, etc.) nor evaluate the simulation results against experimental data. The other investigation is reported by Duran et al.[21] In this study, different hydrodynamic models (laminar, realizable k-ε, and Reynolds stress models [RSMs]) were evaluated in terms of their external mass transfer and photocatalytic oxidation prediction capabilities. A flat-plate differential reactor and formic acid as a model compound were used in the evaluation. Based on radiation field simulations of the system, the UV irradiance over the photocatalyst plates in the reactor was assumed constant. As a consequence, irradiance modeling was excluded from the model and was not evaluated. The study showed good agreement between the model predictions, and the experimental data for those cases where completely laminar or turbulent flow regimens were present in the system.

The primary objective of this study was to develop and evaluate experimentally a CFD-based model for the simulation of photocatalytic reactors, comprising of nanosize TiO_2-coated surfaces used for water treatment. The computational model integrates hydrodynamics, species mass transport, chemical reaction kinetics, and irradiance distribution within the reactor. Each of these aspects have been individually analyzed and experimentally evaluated in previous investigations.[22–25] Two annular reactors presenting different inlet configurations, dimensions, and lamp sizes were used for the experimental evaluation. Benzoic acid (BA) was chosen as a model pollutant, and the CFD-based model was evaluated over a wide range of hydrodynamic conditions ($350 < \mathrm{Re} < 11{,}000$) in which laminar, transient, and turbulent flow regimes were present. Comprehensive methodologies were followed to obtain accurate estimations of the experimental surface reaction rate kinetics and UV lamp power outputs. The model predictions using different hydrodynamic models and near-wall modeling approaches were compared against the experimental data collected. Commercial CFD code Fluent® 6.3.26 was used to perform the simulations.

CFD Model

Laminar flow governing equations

Assuming that the fluid is Newtonian, incompressible, isothermal, non-reactive, with constant physical properties and under laminar steady state flow, the hydrodynamic and species transport governing equations are as follows:[10]

Mass conservation equation:

$$\nabla \cdot (U) = 0 \tag{1}$$

Momentum conservation equation:

$$\nabla \cdot (\rho UU) = -\nabla P - \nabla \cdot \tau \tag{2}$$

where the stress tensor is:

$$\tau = \mu\left(\nabla U + \nabla U^T\right) - \frac{2}{3}\mu \nabla \cdot UI \tag{3}$$

Species conservation equation:

$$\nabla \cdot (\rho U \mathrm{m}_i) = -\nabla \cdot J_i \quad i = 1, 2, \ldots, N-1 \tag{4}$$

where the diffusive flux of species i is estimated using Fick's first law of diffusion:

$$J_i = -D_{\mathrm{m}} \nabla (\rho m_i) \tag{5}$$

In Eqs. 1–5, ρ is density, U is velocity, P is pressure, τ is viscous stress tensor, μ is molecular viscosity, I is unit tensor, m_i is mass fraction of species i, J_i is diffusive flux of species i, N is the total number of species, and D_{m} is the molecular diffusivity of species i in the mixture.

Turbulent flow governing equations

Under the same assumptions stated for the laminar flow model, the Reynolds-averaged Navier-Stokes turbulence modeling approach involves solving the following time-average equations:[10]

Mass conservation equation:

$$\nabla \cdot \left(\overline{U}\right) = 0 \tag{6}$$

Momentum conservation equation:

$$\nabla \cdot \left(\rho \overline{UU} + \rho \overline{uu}\right) = -\nabla \overline{P} - \nabla \cdot \overline{\tau} \tag{7}$$

Species conservation equation:

$$\nabla \cdot \left(\rho \overline{U}\overline{m_i} + \rho \overline{u m_i'}\right) = -\nabla \cdot \overline{J}_i \quad i = 1, 2, \ldots, N-1 \tag{8}$$

where the overbar indicates a time-averaged value, and u and m_i' are fluctuating flow velocity and mass fraction of species i, respectively.

The specification of the apparent stress gradients ($\rho\overline{\boldsymbol{uu}}$) was made by means of a turbulence model.[26–27] Because no turbulence model is universally accepted to be superior for all conditions, four hydrodynamic turbulence models were evaluated against experimental results in this investigation: the widely used standard k–ε model (S k–ε),[28] the realizable k–ε model (R k–ε),[29] the RSM,[30] and the low Reynolds number k–ε turbulence model developed by Abe, Kondoh, and Nagano (AKN).[31] Near-wall modeling for the S k–ε, R k–ε and RSM models were performed with the enhanced wall treatment approach, which combines a two-layer model applicable in regions with fine near-wall meshes, with enhanced wall functions used in regions with coarse meshes.[32] On the other hand, the AKN near-wall modeling approach incorporates wall-damping effects on the empirical constants and functions in the turbulence transport equations. This approach enables the extension of the k–ε turbulence model all the way to the wall. The AKN model has given promising results in modeling near-wall heat and mass transfers in various applications,[33–34] and more recently modeling external mass transfer[23] and surface reaction[24] in annular reactors.

The specification of the mass transfer fluxes ($\rho\overline{um_i'}$) was made by analogy to the linear approximation for the Reynolds stresses (or to Fick's first law of diffusion):

$$\rho\overline{um_i'} = -D_t\nabla(\rho\overline{m_i}) \tag{9}$$

where D_t is the so-called eddy (or turbulent) diffusivity for species concentration. Combining Eqs. 5, 8, and 9 results in the convection-diffusion turbulent mass transfer equation applicable to our case:

$$\nabla\cdot\left(\rho\overline{Um_i}\right) = \nabla\cdot\left[\left(\rho D_m + \frac{\mu_t}{Sc_t}\right)\nabla\overline{m_i}\right] \tag{10}$$

with Sc_t, the turbulent Schmidt number, defined as the ratio between the turbulent viscosity, μ_t, and the turbulent diffusivity:

$$Sc_t = \frac{\mu_t}{\rho D_t} \tag{11}$$

A value of $Sc_t = 0.7$ was used in the simulations as recommended in various references.[35–36]

Radiation field governing equations

Modeling the radiation field in a given photoreactor involves solving the radiative (photon) transfer equation (RTE).[37–38] For monochromatic radiation, the RTE is defined as:

$$\frac{dL(r,s)}{dz} + (\kappa+\sigma)L(r,s) = j^e(r) + \frac{\sigma}{4\pi}\int_{4\pi} L(r,s')p(s'\to s)d\Omega' \tag{12}$$

where L is the photon radiance, r is the position vector, s is the propagation direction vector, z is the path length, κ is the absorption coefficient, σ is the scattering coefficient, j^e is the emission (source) term, p is the phase function for the in-scattering of photons, and Ω' is the solid angle about the scattering direction vector s'. Fluent solves the RTE using the finite volume method which considers the RTE in the direction s as a field equation;[38] thus, Eq. 12 is rewritten and solved as:

$$\nabla\cdot(L(r,s)s) + (\kappa+\sigma)L(r,s) = \kappa n^2\frac{\sigma_{S-B}T^4}{\pi} + \frac{\sigma}{4\pi}\int_{4\pi} L(r,s')p(s'\to s)d\Omega' \tag{13}$$

where n is the refractive index, $\sigma_{S\text{-}B}$ is the Stefan-Boltzmann constant (5.672×10^{-8} W m^{-2} K^{-4}), and T is the absolute temperature of the medium.

In this investigation, the reactor monochromatic lamp was included in the computational domain. The lamp emission model implemented was a modification of the extensive source volumetric emission model[37] that incorporates the photon absorbance/re-emission effect produced by the mercury vapor in the lamp, so as the reflection/refraction/absorption at the lamp quartz envelope (ESVERA model). All the details about this lamp emission model and its corresponding CFD-based modeling approach can be found elsewhere.[25]

Surface chemistry model

The heterogeneous photocatalytic decomposition of BA over a composite sol-gel TiO_2 coating was selected as the model reaction for the experimental evaluation of the developed CFD-based model. Photocatalytic reactions carried out in a porous photocatalyst layer are "volumetric" reactions. The rates of these reactions vary with position within the layer because of UV irradiance gradients caused by radiation absorption and concentration gradients of the reacting species caused by conversion or diffusion resistance.[39] However, the overall reaction can be treated as an surface reaction by expressing the overall degradation reaction rate (free of external mass transfer limitation) in per unit area of coated catalyst. This overall reaction rate is a function of the concentration of the reacting species and UV irradiance at the liquid-catalyst layer interface, and of a series of properties inherent to the catalyst layer (i.e., UV absorption coefficient, thickness, tortuosity, porosity, etc.).[39–41]

Under the experimental conditions used in this study, the surface photocatalytic decomposition of BA $-R_{BA}^S$ followed pseudo first-order kinetics with respect to the concentration of BA and the UV irradiance (refer to the kinetics determination experiments in the "Results and Discussion" section). Thus, the rate expression was defined by:

$$-R_{BA}^S = M_W\alpha E C_{BA,S} \tag{14}$$

where M_W is the BA molar weight, α is the rate constant obtained from the kinetic experiments, E is the UV irradiance reaching the catalyst surface, and $C_{BA,S}$ is the BA molar concentration at the catalyst surface exposed to the fluid medium. α is inherent to the photocatalyst coating, BA initial concentration, and dissolved oxygen concentration used in the experiments; in this study an α value of 4.75×10^{-6} m^3 W^{-1} s^{-1} was obtained. This reaction rate expression (Eq. 14) was

programmed as a sub-program (user defined function in Fluent), and it was integrated to the surface reaction rate model of Fluent. Because an overall reaction is required to be set in the CFD software, complete mineralization of BA was assumed ($C_6H_5COOH + 15/2\ O_2 \rightarrow 7\ CO_2 + 3\ H_2O$). The "laminar finite rate" model which ignores the effect of turbulent fluctuations on reaction rates was chosen for reaction modeling.

Geometrical models and mesh structure

Two commonly used annular reactor configurations were studied, with the inlet normal (U-shape) and parallel (L-shape) to the main reactor body. The reactor geometries are shown with their dimensions in Figure 1. The inlet and outlet tubes were chosen to be 100 diameters in length to ensure that a fully developed flow was established at the entrance and at the outlet boundaries of the reactor. The L-shape reactor sleeve holder consisted of three prongs (3-mm wide $\times$ 5.5-mm long $\times$ 3-mm thick) located 120° one from another.

A boundary-layer mesh was setup in the annular region where the surface reaction took place. $y^+ < 0.5$ at the wall-adjacent cell, and at least 10 cells within the viscosity-affected near-wall region ($Re_y < 200$) were defined.[23] Also, a boundary-layer mesh was setup at the lamp envelope where high radiation gradients occur. The commercial mesh generator Gambit® 2.2.30 was used to create the grid. Structured hexahedral cells were used to discretize the physical domains, except for the region of the sleeve holder of the L-shape reactor, where it was necessary to split the reactor domain and use unstructured cells. The used grids had approximately 1.7 million volume cells, and they were verified to give mesh-independent results.

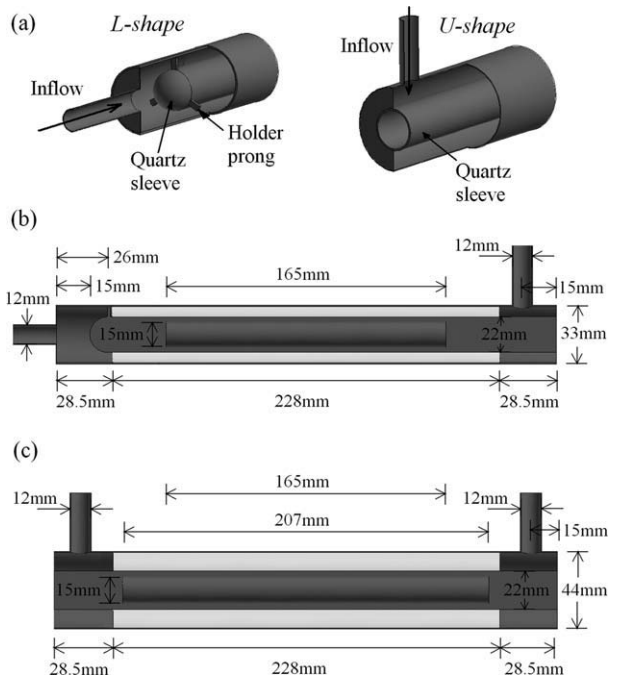

Figure 1. Schematic diagram and dimensions of the U-shape and L-shape TiO_2-coated annular reactors: (a) reactor entrance details, (b) L-shape reactor dimensions, (c) U-shape reactor dimensions (with two UV lamp lengths of 165 and 207 mm).

The 228-mm-long white areas shown in both reactors correspond to the photocatalyst coatings. The cylinders inside the sleeves represent the UV lamps.

Boundary conditions

The boundary conditions related to the hydrodynamics and mass transport in the CFD model were defined as follows. At the inlet, the mass flow rate of the fluid was specified. The direction of the flow was defined normal to the boundary. For the cases corresponding to turbulent flow, the hydraulic diameter was fixed at 12 mm, and the turbulence intensity (TI) was set according to the formula $TI = 0.16\ Re^{-1/8}$.[32] The inlet mass fractions of BA, dissolved oxygen, and carbon dioxide were specified as 4.41×10^{-6}, 8.0×10^{-6}, and 0, respectively. These conditions were defined considering that in a typical experimental run, the initial concentration of BA was around 4.41 ppm, the dissolved oxygen concentration was kept constant at saturation (8 ppm at 25°C) and no CO_2 was present initially. At the outlet, a fully developed flow (outflow) condition was applied. At all the walls, a no-slip boundary condition was imposed. Also, zero diffusive flux of species was specified at the walls, except for the walls coated with the photocatalyst where the following boundary condition was defined:

$$J_i \cdot \hat{n} = R_i^S \tag{15}$$

where $\hat{n}$ is the unit vector normal to the surface, and R_i^S is the rate of production/depletion of species i arising from the surface.

The radiation field boundary conditions were defined as follows. The lamp plasma was defined as a solid continuum cylinder surrounded by a 1-mm thick, semitransparent, fully specular wall. The temperature of the entire computational domain was set at 1 K (to eliminate any volumetric radiation effect), except for the temperature of the lamp plasma which was defined so that the radiation power generated matched the corresponding power output of the lamp. The lamp end caps were semitransparent, fully diffused absorbent walls. The air surrounding the lamp was also defined as a solid continuum. The quartz sleeve was set as a 1-mm thick, semitransparent, and fully specular wall. The water inside the annulus was defined as a fluid continuum, and all the remaining walls (including the photocatalyst-coated wall) were set as zero-thickness, opaque, fully diffused, non-reflective walls. A detailed explanation of these radiation field boundary conditions can be found elsewhere.[25]

Physical properties

The concentrations of BA used in this study were very low (<5 mg/L); consequently, the physical properties of water were assumed for the solution. At 298 K, the following values were used:[42–44] $\mu = 8.9 \times 10^{-4}$ Pa·s, $\rho = 997$ kg/m^3, $D_m = 9.32 \times 10^{-10}$ m^2/s, $n = 1.38$, and $\kappa = 1.3$ m^{-1} (measured for a 2.5 ppm BA solution). The optical

properties assumed for the other materials were as follows: air ($n = 1.00$, and $\kappa = 0\ m^{-1}$), GE 124 quartz[42,45] ($n = 1.52$, and $\kappa = 22\ m^{-1}$), lamp plasma[46] ($n = 1.00$, and $\kappa = 191\ m^{-1}$). All the optical properties were estimated for 254 nm UV radiation.

Numerical solution method and strategy

Commercial CFD code Fluent® 6.3.26 was used to perform the simulations. The segregated steady-state solver was used to solve the governing equations. Second-order upwind discretization scheme was used except for pressure for which the standard scheme was selected. The SIMPLE algorithm was chosen for the pressure-velocity coupling. An angular discretization of 40 divisions was used for solving the RTE. This number was found to be sufficient to avoid the appearance of the "ray effect"; and to overcome control angle overhang, 1 × 1 pixelation was used.[47–48] Convergence of the numerical solution was assured by monitoring the scaled residuals to a criterion of at least 10^{-4} for the continuity and momentum, and 10^{-6} for the concentration and radiation variables. In addition, the variation of velocity magnitude, BA concentration, and radiation fluence rate at several points of the computational domain was used as an indicator of convergence.

Taking advantage of the facts that in the studied system the velocity and radiation fields did not interact, and that the photocatalytic reaction development did not affect these fields, the CFD model was solved in three steps. First, the equations of conservation of mass and momentum were solved for getting the flow field across the computational domain. Then, the velocity values were kept "frozen," and the RTE was solved for obtaining the radiation field. Finally, keeping "frozen" the converged flow and radiation field solutions, the conservation of species equation was solved for computing the BA concentration map within the system. This solving strategy saves computation time and brings stability to the solution.

Experimental

Catalyst preparation

The photocatalyst used in the experiments was a composite sol-gel TiO_2 coating. A detailed description of the steps followed in the preparation of the composite sol-gel TiO_2 coating can be found elsewhere.[49] The titanium tetraisopropoxide (97%) was from Sigma-Aldrich; the HCl (36.5%) and denatured ethanol (85% ethanol+15% methanol) from Fisher Sci.; and the TiO_2 power was Degussa P-25. The prepared mixture was deposited on the desired surfaces (previously sandblasted to improve the adhesion of the coating) using dip-coating technique at a withdrawal speed of 1.25 cm/min. The coated samples were dried at room temperature for 1 h and then heat-treated at 500°C for 2 h. Under the used conditions, the resulting coating density was estimated gravimetrically at $17.3 \pm 1.7\ g/m^2$.

Determination of the surface reaction kinetics

For obtaining the surface kinetics, experiments were conducted in a differential reactor (i.e., a reactor with very low conversion per pass) equipped with three glass slides (25 mm × 75 mm each) coated with the photocatalyst according to the previously described method. The reactor consisted of a 63-mm wide aluminum block designed to allow the BA solution to flow through a 225-mm long passage of 25 mm (width) and 3 mm (height), and over the coated glass plates. The reactor was covered by a diffused quartz plate and was irradiated by two low-pressure mercury UV lamps (GPH357T5L/4P, Atlantic Ultraviolet) mounted under an aluminum reflector. Radiometer measurements and irradiance CFD simulations reported elsewhere[21] demonstrated that the irradiance over the coated glass slides was fairly uniform; therefore, a constant value could be assumed. Schematics of the experimental setup can be found in the cited study.[21] The differential reactor was operated in a constantly aerated, recirculating batch system. Five hundred milliliters of BA solution (prepared using ACS certified BA from Fisher Sci. and ultrapure water) with an initial concentration of ~5 mg/L was charged in a mixed tank (600 mL glass beaker), and then pumped through the reactor using a magnetic drive gear pump (Micropump 221/56C). The solution was run for 30 min without UV irradiation for BA absorption equilibrium to occur; after which, samples were collected from the well mixed tank every 20 min over a period of 120 min, and their BA concentration was analyzed.

The previous procedure was repeated for different UV irradiance values which were adjusted by changing the distance of the UV lamps to the reactor. The lamp centerlines (20 mm away from each other) were located 5, 10, 15, 22.5, and 30 cm above the quartz plate. The UV irradiance over the catalyst-coated slides was measured using potassium ferrioxalate actinometry. For this, 500 mL of potassium ferrioxalate solution (0.02 M), prepared and used as described by Murov et al.,[50] was recirculated through the differential reactor without TiO_2-coated slides. All the chemicals used were ACS certified, obtained from Fisher Sci., and used as received. The reactor quartz plate was covered with UV absorbent electrical tape (3M) except for the area above the normal position of the coated glass slides. Samples were taken from the container beaker at different time intervals, and the irradiance was calculated with the following formula:[50–51]

$$E = \frac{4.72 \times 10^5 \times V_T}{\Phi \times A} \times \frac{dC_{Fe^{2+}}}{dt} \times 0.89 \qquad (16)$$

where V_T is the total volume of liquid solution, Φ is the quantum yield of potassium ferrioxalate at 254 nm, A is the area of the irradiated window (which corresponds to the area of the coated slides), dC_{Fe}^{2+}/dt is the slope obtained from the linear regression of Fe^{2+}-concentration versus time, 4.72×10^5 is a factor to convert Einstein to Joule (valid for 254 nm radiation), and 0.89 is a correction factor to deduct the contributions made by the lamp emitted radiation having wavelengths longer than 254 nm.[52] The quantum yield used in the calculations was $\Phi = 1.41$ in accordance with a recent study by Goldstein and Rabani.[53]

Photocatalytic degradation performance of the annular reactors

The CFD-based model was evaluated against the experimental performance of annular reactor prototypes having the

Figure 2. TiO_2-coated U-shape annular reactor used in the experiments.

(a) photocatalyst-coated glass halves, (b) photocatalyst-coated glass tube fitted in the PVC structure, and (c) U-shape annular reactor under operation. A similar reactor with modified inlet was used for the L-shape geometry. [Color figure can be viewed in the online issue, which is available at wileyonlinelibrary.com.]

same dimensions as the geometrical models described in Figure 1. The reactor structures were made of PVC and included a union that allowed for fitting catalyst-coated glass tubes in the inside (see Figure 2). The TiO_2 photocatalyst was coated on the inner wall of previously sand blasted glass tube halves (76-mm long and 33- or 44-mm inner diameter) as shown in Figure 2a. Six tube halves were put together using electrical tape to form 228-mm long coated tubes with either 33 or 44 mm inner diameter. The reactor quartz sleeves had 20 mm inner diameter and 1.0 mm wall thickness (quartz type GE 124, CANSCI Glass Products Ltd.). The L-shape reactor was operated using a 165 mm-long lamp, whereas the U-shape reactor was operated using two different lamps (165 and 207 mm). With the low-pressure mercury lamps (GPH357T5L/4P, Light Sources Inc.) having 277 mm arc lengths, the desired lamp lengths (165 and 207 mm) were obtained by covering the ends of the lamps with a layer of Teflon tape, topped by another layer of electrical tape.

The UV power output of the lamps under the actual operating conditions in the reactors was estimated as follows. First, the output of the lamps running in air was determined using the method proposed by Lawal et al.[54] For this, the irradiance at 1 m perpendicular to the center of a lamp was measured using a radiometer (IL1700, SED240 detector, NS254filter, International Light Tech.). Under these conditions, the power output (W) was calculated using the following formula:

$$W = \frac{E2\pi^2 y \times l}{2\beta + \sin 2\beta} \tag{17}$$

where y is the normal distance from the lamp, l is the lamp length, and β is the half angle subtended by the lamp at the sensor position (i.e., $\tan \beta = l/(2y)$). The power values obtained in air at 21°C were corrected to the operating conditions inside the reactor quartz sleeve surrounded by water at 25°C. For this, a temperature correction factor of 0.975 as obtained in a separate study was used.[25]

The TiO_2-coated annular reactors were operated in recirculating batch mode using the experimental setup shown schematically in Figure 3. The tank was a 3 L plastic beaker, and the pump was a magnetic drive centrifugal pump (Flotec MDR6OT-X03). The temperature of the system was kept at 298.0 K ± 0.5 K and was measured using a type-K thermocouple system (Digi-Sense, Cole-Parmer). Temperature control was achieved passing cold water through a copper coil submerged in the tank. The operation of the system involved recirculating 2.5 L of constantly aerated BA solution (initial concentration ~5 mg/L) at constant flow rate through the reactor. At the beginning of each experiment, the solution was

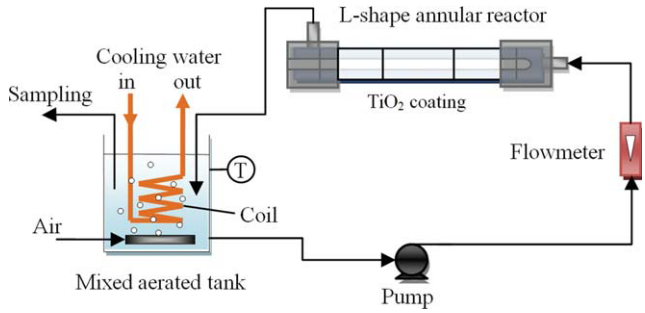

Figure 3. Schematic of the experimental setup used for evaluating the photocatalytic degradation performance of the prototype annular reactors.

[Color figure can be viewed in the online issue, which is available at wileyonlinelibrary.com.]

run for 30 min without UV irradiation for BA absorption equilibrium to occur. Following, the UV lamp (preoperated for 30 min to achieve stabilized emission) was inserted in the reactor sleeve, and samples were taken from the tank every 15 min for 90 min. The samples were analyzed for their BA content. The procedure was repeated using flow rates of 1.0, 6.6, 11.4, and 24.6 L/min for the L-shape reactor and 1.0, 8.5, 20.0, and 27.4 L/min for the U-shape reactor.

Analytical methods

The concentration of Fe^{2+} formed during the actinometric measurements was determined via UV spectrophotometry at 510 nm (Cary 100 UV-Visible spectrophotometer, Varian).[50] The concentration of BA was directly analyzed with a Waters 2695 HPLC. Separation was accomplished using a reverse phase Nova Pak C18 4 μm 3.9 $\times$ 150 mm separator column operated at 35°C. The compound detection was achieved using a Waters 2998 photodiode array detector with UV detection (detection wavelength = 230 nm). A sample volume of 100 μL was injected to the system and a 58% methanol/40% water/2% acetic acid solution was used as the mobile phase. The type of elution was isocratic with a flow rate of 1.23 mL/min. Empower Pro software was used to analyze the chromatographs.

Results and Discussion

Surface reaction kinetics

Before investigating the surface kinetics of the photocatalytic reaction of BA, experiments were conducted to study any possible removal of the model pollutant by direct photolysis and/or adsorption on to the photocatalyst surface. The direct photolysis experiments showed a small degradation of BA (<15% in 2 h) that presented first-order kinetics. On the other hand, only a small fraction of the initial BA (<5%) was adsorbed on the TiO_2 coating within the first 20 min of contact time.

Several runs at different UV irradiances and flow rates were performed in the differential reactor, each resulting in an exponential decay of BA concentration with time. This observed exponential decay implied that the surface reaction rate follows first-order kinetics with respect to the BA concentration.[24] However, a dependence of the photocatalytic degradation rate on the flow rate was also observed, implying that the reaction rate was being partially limited by the rate of external mass transfer in the system. As a consequence, the surface reaction rate constants (k'') were calculated using the BA external mass transfer coefficients for the used system reported in a previous study[21] according to:[55]

$$k'' = \frac{k''_{\text{eff}} \times k_c}{k_c - k''_{\text{eff}}} \tag{18}$$

where k''_{eff} is the effective surface reaction rate constant, and k_c is the mass transfer coefficient for experiments performed using a flow rate of 5 L/min. k''_{eff} was obtained subtracting the rate constant associated with direct photolysis from the observed reaction rate constant. Figure 4 shows the surface reaction rate constants obtained for different UV irradiances. The surface reaction rate constants presented a linear relationship with the UV irradiance ($k'' = 4.75 \times 10^{-6} E$); and overall, the molar photocatalytic degradation rate of BA ($-r''_{\text{BA}}$) followed first-order kinetics with respect to BA concentration and UV irradiance at the photocatalyst surface layer:

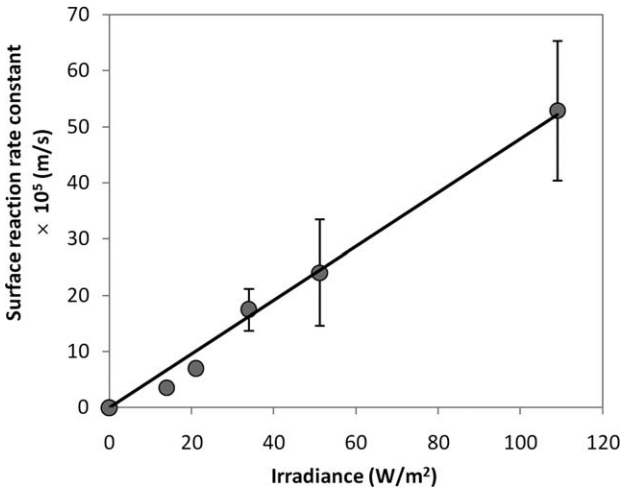

Figure 4. Surface reaction rate constants obtained at different UV irradiances for the photocatalytic degradation of BA over the composite sol-gel TiO_2 coating.

The error bars represent the 95% confidence intervals.

$$-r_{\text{BA}} = 4.75 \times 10^{-6} \times E \times C_{\text{BA,S}} \tag{19}$$

Heterogeneous photocatalytic reactions of diluted substrate solutions with constant dissolved oxygen concentration are commonly found to follow pseudo first-order kinetics with respect to the substrate concentration.[56–57] Also, linear dependence of the reaction rate with the UV irradiance is normally reported for systems under low UV irradiation.[5,58] For the particular case of BA, analogous results were reported in another investigation in which the concentration and irradiance conditions were similar to the ones used in this work.[59]

It is worth noting that even though the surface reaction rate expression (Eq. 19) does not correspond to the intrinsic reaction kinetics, it is inherent to the photocatalyst coating and dissolved oxygen concentration used in the kinetic experiments.[39–41,60] Therefore, it is expected that this surface reaction kinetic expression can be used for predicting the BA degradation rate in any other immobilized system which uses the same TiO_2 coating (same preparation, coating technique, coating thickness) and dissolved oxygen concentration as in here. Similar methodology presented here can be applied to determine the surface kinetic expression for other conditions.

CFD simulations of the prototype annular reactors

Besides the surface kinetics expression, the other required experimental parameter for running the CFD simulations was the lamp power outputs. Because of the importance of this parameter, the comprehensive methodology described in the Experimental section was used for obtaining reliable values. After this method, the UV output of the 165 and 207 mm lamps were estimated to be 3.3 and 4.1 W, respectively.

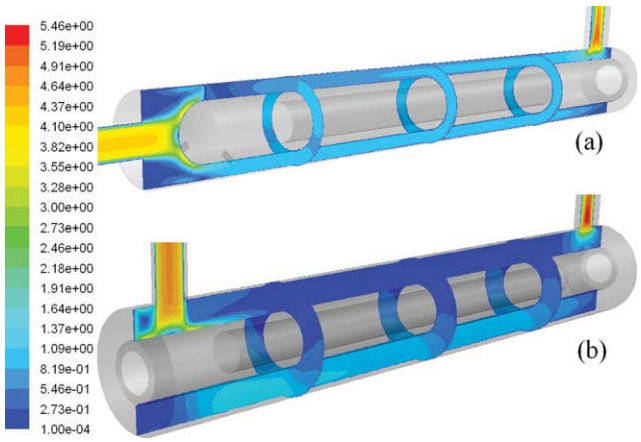

Figure 5. Contours of velocity magnitude (m/s) in the L-shape (a) and U-shape (b) annular reactors calculated using the AKN turbulence model.

The figure shows the longitudinal center plane and three transversal planes along the reactor volume. The results correspond to flow rates of 24.6 L/min (Re = 11,000) and 27.4 L/min (Re = 10,000), respectively. [Color figure can be viewed in the online issue, which is available at wileyonlinelibrary.com.]

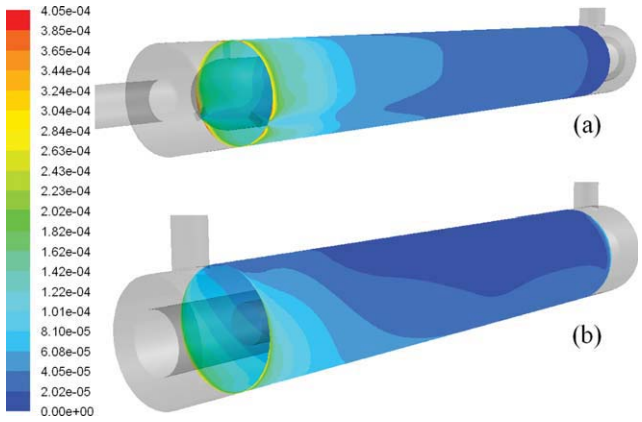

Figure 6. Local mass transfer coefficient distributions (m/s) on the photocatalyst surface of the L-shape (a) and U-shape (b) annular reactors as calculated using the AKN turbulence model.

The results correspond to flow rates of 24.6 L/min (Re = 11,000) and 27.4 L/min (Re = 10,000), respectively. [Color figure can be viewed in the online issue, which is available at wileyonlinelibrary.com.]

Steady state CFD simulations of the prototype annular reactors were performed using different hydrodynamic models. Several operating flow rates which represented $350 < \mathrm{Re} < 11{,}000$ were used to cover a range of laminar, transitional, and turbulent flow conditions. Even though the absolute values of the obtained results were different for each of the flow rates and turbulence models evaluated, the main patterns and local distributions of the analyzed variables (velocity, mass transfer coefficient, surface reaction rate, and external effectiveness factor) were somehow similar. These general results are described in the following paragraphs.

The obtained hydrodynamic results (Figure 5) were very similar to the ones obtained in previous investigations of annular reactors.[22–23] Essentially, the velocity magnitude distribution along the annular space was more uniform for the L-shape than for the U-shape configuration. In the U-shape reactor, the fluid presented high velocities in the section opposite to the inlet and outlet ports, but low velocities on the same side of the ports. In the case of the L-shape reactor, the inner tube holder prongs generated a wake of low velocity behind them. These velocity distributions induced analogous local mass transfer coefficient distributions on the photocatalyst-coated surfaces, as presented in Figure 6. The local mass transfer coefficients were calculated in Fluent using a custom field function defined as:

$$k_c = \frac{4.75 \times 10^{-6} E \times C_{BA,S}}{C_{BA,B} - C_{BA,S}} \tag{20}$$

where $C_{BA,B}$ is the concentration of BA in the bulk fluid (assumed equal to the inlet concentration because of the small conversion of BA). Equation 20 is obtained from equating the surface reaction rate and the mass transport flux; this derives from the steady state assumption used for solving the governing equations.

The local distribution of mass transfer coefficients is very valuable for analyzing the performance of immobilized photocatalytic reactors. The overall reaction rate in these systems is usually limited by the rate of mass transport. Hence, identifying areas of low mass transfer, and finding alternatives for increasing the transport of species toward those photocatalyst-coated areas will result in an increase of the degradation rate achieved in the photoreactor. For example, the U-shape annular reactor configuration presents a low mass transfer area in the top region of the reactor, toward the outlet port (see Figure 6b). This situation could be improved, for example, with the insertion of internal baffles that generate fluid turbulence toward that region.

The results of the radiation field simulations are presented in terms of irradiance distributions over the TiO_2-coated surface in Figure 7. Because of the proximity between the

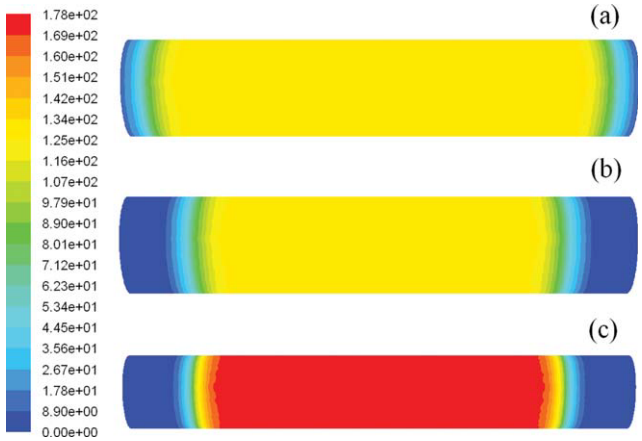

Figure 7. Irradiance distributions (W/m^2) over the TiO_2-photocatalyst surface for: (a) U-shape reactor with 207-mm lamp, (b) U-shape reactor with 165-mm lamp, and (c) L-shape reactor with 165-mm lamp.

[Color figure can be viewed in the online issue, which is available at wileyonlinelibrary.com.]

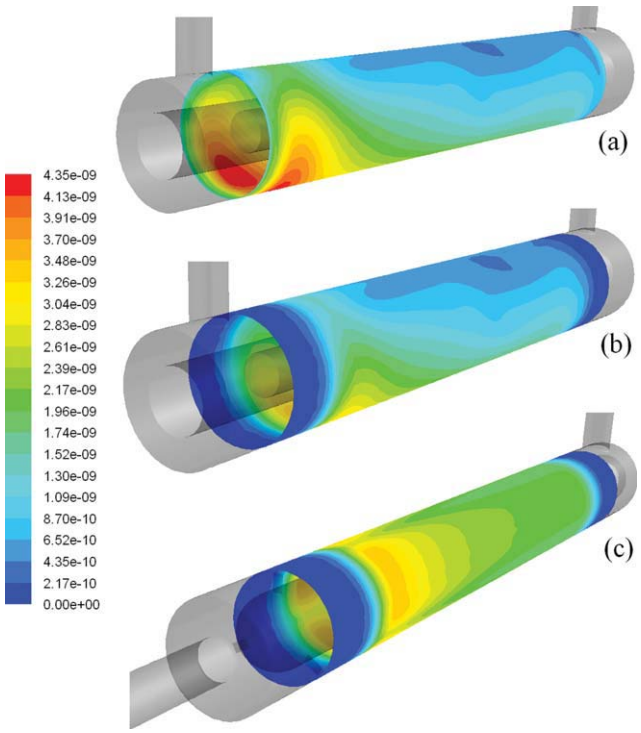

Figure 8. Surface reaction rate (kmol s^{-1} m^{-2}) distributions over the TiO_2-photocatalyst surface for: (a) U-shape reactor with 207-mm lamp, (b) U-shape reactor with 165-mm lamp, and (c) L-shape reactor with 165-mm lamp.

The results were computed using the AKN turbulence model for flow rates of 24.6 L/min (L-shape reactor) and 27.4 L/min (U-shape reactors). [Color figure can be viewed in the online issue, which is available at wileyonlinelibrary.com.]

photocatalyst surface and the lamps (<1.5 cm), the predicted irradiance profiles were nearly flat in the regions directly facing the lamps and then dropped drastically toward the ends of the coated-areas. These results agree with the experimental measurements of irradiance at the outer wall of an annular reactor reported elsewhere.[25] As seen in Figure 7, the irradiance distributions and irradiance values on the photocatalyst layer of each reactor are very specific. For example, the irradiance values at the cental area of the reactors (areas with the highest irradiance) present differences of up to 50%. Evaluating the CFD model at different UV irradiance values and distributions is very important since during scale-up these quantities usually change.

Figure 8 presents the local surface reaction rate distributions over the photocatalyst surface. As expected, the areas combining high velocity gradients (and therefore, high mass transfer coefficients) with high UV irradiance resulted in high surface reaction rate, whereas low surface reaction rates were found in the areas having low mass transport and/or UV irradiance. The U-shape reactor with the 207 mm lamp (Figure 8a) showed high surface reaction rates at the entrance region, particularly at the bottom of the annular space where the incoming fluid presented high velocity gradients. However, as expected from the local mass transfer analysis, this reactor showed low reaction rates in the top, outlet area. The U-shape reactor with the 165-mm lamp (Figure 8b) presented a similar behavior, except for the two ends of the TiO_2-coated surface where the reaction rate was minimal because of the absence of sufficient UV irradiation. The L-shape reactor with the 165-mm lamp presented overall higher surface reaction rates because of the more uniform velocity and mass transfer distributions. However, regardless of mass transfer rates, the surface reaction rates at the end sections of the catalyst were close to zero because of the very low UV irradiance reaching the photocatalyst in those regions.

The external effectiveness factor (E_{ex}) demonstrated to be a suitable parameter for analyzing the performance of turbulence and near-wall models in terms of their surface reaction prediction capabilities.[24] This factor is defined as the ratio between the observed reaction rate and the reaction rate without external mass transport limitations.[61] In this work, E_{ex} was computed using a custom field function in Fluent as follows:

$$E_{ex} = \frac{k'' C_{BA,S}}{k'' C_{BA,B}} = \frac{C_{BA,S}}{C_{BA,B}} \tag{21}$$

Figure 9 presents the local effectiveness factor distributions obtained for the analyzed annular reactors. The magnitude of E_{ex} ranges from 0 to 1, indicating the relative importance of diffusion and reaction limitations. As E_{ex} approaches 1, the overall reaction is surface-reaction-limited,

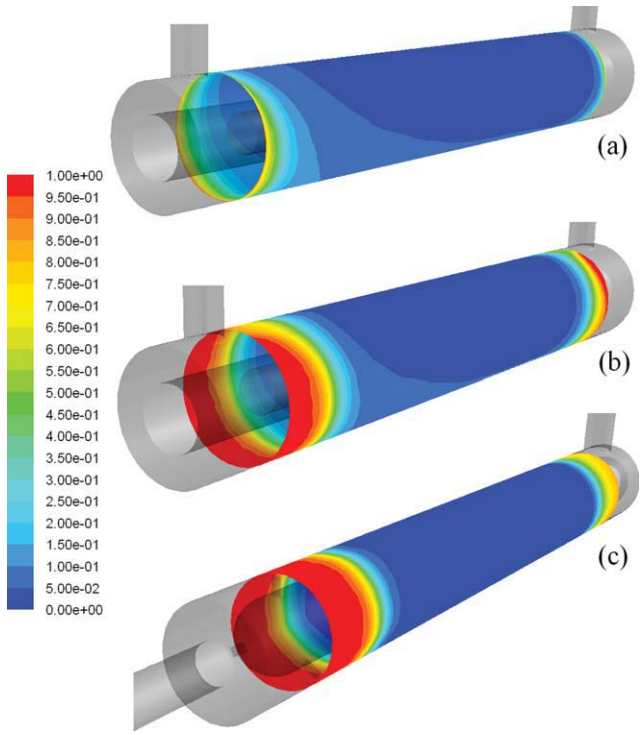

Figure 9. External effectiveness factor (dimensionless) distributions over the TiO_2-photocatalyst surface for: (a) U-shape reactor with 207-mm lamp, (b) U-shape reactor with 165-mm lamp, and (c) L-shape reactor with 165-mm lamp.

The results were computed using the AKN turbulence model for flow rates of 24.6 L/min (L-shape reactor) and 27.4 L/min (U-shape reactors). [Color figure can be viewed in the online issue, which is available at wileyonlinelibrary.com.]

whereas when E_{ex} is much smaller than 1 (i.e., $E_{ex} < 1$), the overall reaction is diffusion limited. A common criterion applied to heterogeneous reactions states that if E_{ex} is larger than 0.95, external mass transport limitation is negligible in the system.[61] The analysis of the local E_{ex} distributions in the three reactors shown in Figure 9 reveals that E_{ex} was very low at those areas where surface reaction was taking place (areas with significant UV irradiance). This result implies that at those regions, the surface reaction rate was much higher than the mass transport rate which induced overall a diffusion controlled process. E_{ex} values close to 1 were achieved only at the end sections of the catalyst surface for the 165-mm lamp reactors, where the surface reaction rates were very low because of the lack of UV irradiation. These results confirm that overall, the pollutant degradation rates in immobilized photocatalytic reactors are strongly limited by external mass transfer. In such systems, the prediction of the overall reactor performance will be largely determined by the external mass transfer prediction capabilities of the hydrodynamic models used for the simulations.[24]

Comparison of the CFD simulations with the reactor experimental performances

Several runs at different flow rates were performed, operating the immobilized photocatalytic reactor prototypes in recirculating batch mode. The photocatalytic degradation performance of the reactors was measured in terms of the apparent degradation rate constants (k_{app}) obtained under each experimental condition. These reaction rate constants corresponded to the photocatalytic degradation only and were computed subtracting the direct photolysis rate constants (obtained from control runs without the photocatalyst) from the observed reaction rates. The apparent reaction rate constants obtained from the experiments were compared with the rate constants calculated by the model. The CFD-based apparent rate constants were calculated using the BA conversion per pass (X_S) achieved in the photoreactor as predicted by the steady state CFD simulations. This calculation was based on the analysis presented by Duran et al.[24] which derives from the fact that the conversion per pass, X_S, in any reactor (real or ideal) with first-order reaction kinetics is the same for the reactor operating in either continuous or recirculating batch mode. Given this property, the apparent reaction rate constants for the recirculating system were calculated using the following formula:[24]

$$k_{app} = \frac{X_S}{\theta_T - X_S\theta_R} \tag{22}$$

where θ_T is the total residence time within the system ($\theta_T = V_T/Q$), θ_R is the residence time in the reactor ($\theta_R = V_R/Q$), V_T is the total fluid volume in the system, V_R is the reactor volume, and Q is the flow rate through the reactor. Equation 22 was obtained from a model which describes the dynamic process of the catalytic reaction within the reactor as well as mixing within the holding tank in a recirculating batch system. The detailed model description is provided by Duran et al.[24]

Figure 10 presents the results obtained for each of the prototype reactors and hydrodynamic models evaluated in this work. The experimental apparent reaction rates obtained for

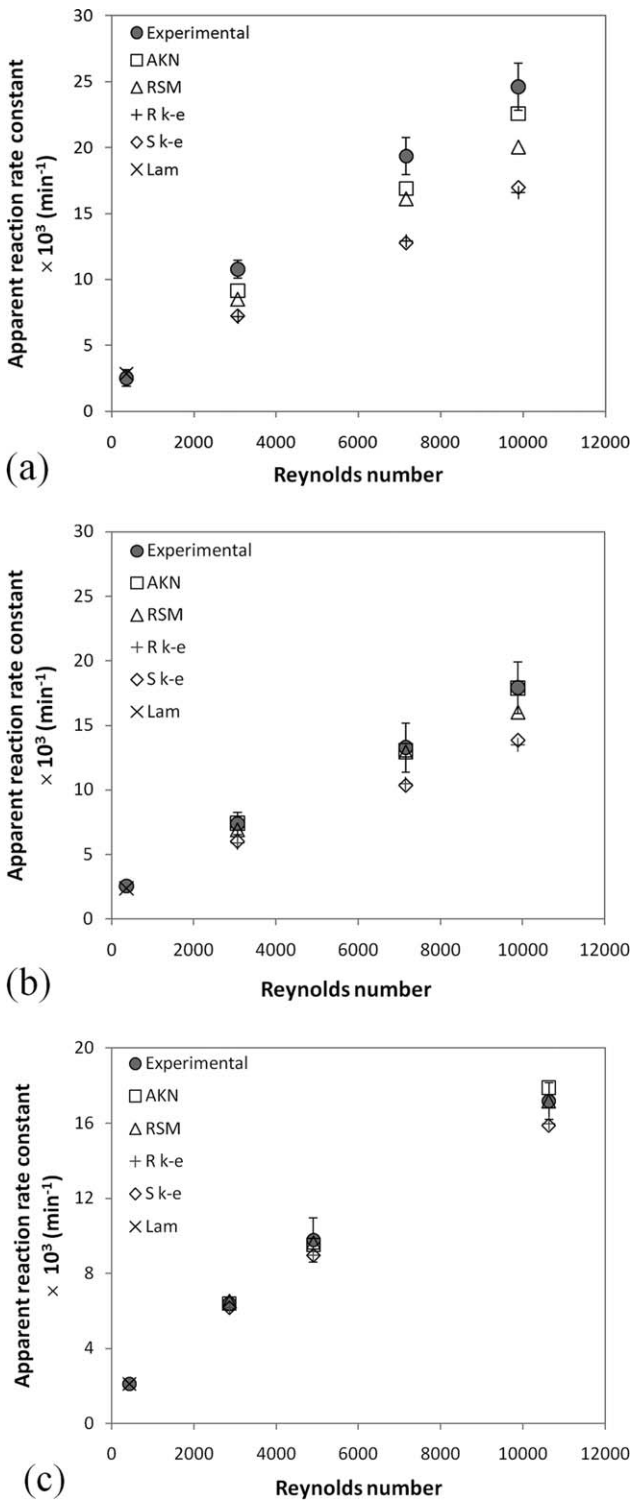

Figure 10. Comparison of the apparent reaction rate constants estimated based on CFD simulations with the ones obtained experimentally for the U-shape reactor with 207 mm lamp (a), U-shape reactor with 165-mm lamp (b), and L-shape reactor with 165-mm lamp (c).

The CFD predictions were computed using different hydrodynamic models and the error bars represent the 95% confidence interval obtained with triplicate runs.

the three reactors presented a monotonic increasing tendency with respect to flow rate. These results confirmed that the overall photocatalytic degradation process was limited by the rate of mass transport within the range of the studied flow rates. When analyzing the performance predictions obtained using different hydrodynamic models, it can be noticed that the laminar model was able to predict the photocatalytic rate for all the studied annular reactors. This result agrees with those of previous studies[11–12,23–24] in which the laminar model presented very good external mass transfer and surface reaction prediction performance.

The prediction performance of the turbulence models was different for each of the photocatalytic reactors. For the U-shape reactor with the 207-mm lamp, all the turbulence models underpredicted, to some extent, the apparent reaction rate constants (Figure 10a). The predictions of the AKN model were in fair agreement with the experimental data (average error = 12%), RSM gave an average error of 19%, and R k-ε and S k-ε presented the largest deviation from the experimental results (average error = 33%). The CFD simulations of the external effectiveness factor for this reactor (see Figure 9a) revealed that the BA degradation process was highly limited (and hence determined) by the rate of mass transfer over the entire photocatalyst surface. Under these conditions, the performance of the turbulence models for predicting the degradation of BA in the reactor was defined by their capability to predict external mass transfer in the system. In this sense, the results presented here are consistent with the ones obtained by Duran et al.[23] in an investigation on external mass transfer prediction capabilities of different hydrodynamic models in annular reactors. According to the cited work, the studied turbulence models underpredicted the average mass transfer; however, AKN model provided better predictions of both average and local mass transfer rates. The overall underprediction was mainly attributed to an inappropriate prediction of mass transfer at the highly turbulent entrance section of the reactors. However, once the flow redeveloped through the annular space, model predictions, particularly those from the AKN and RSM models, improved significantly.

The results obtained for the other two reactors (U-shape and L-shape with 165 mm lamp) can also be discussed in the light of the previous analysis. The external effectiveness factor distribution for these reactors revealed that essentially no reaction, and hence mass transfer, took place at the end sections of the photocatalyst surface because of the absence of UV irradiation (see Figures 9b and c). According to this result, it could be expected that the overall performance of the turbulence models would be better for these reactors since no mass transport took place at the region where the models failed to predict mass transfer (entrance section of the reactor); all the species transport happened at the central region of the reactor where turbulence models perform well predicting mass transfer. As it can be seen in Figures 10b and c, the predictions of the turbulence models were in fact better for both reactors. AKN predictions presented an excellent match with the experimental data, RSM predictions were very close, but R k-ε and S k-ε continued underpredicting, to some extent, the degradation rate of BA.

Overall, AKN model presented better prediction of the degradation rate in the analyzed photocatalytic reactors. The better performance of the AKN model can be attributed to the large impact that near-wall region modeling has on interfacial phenomena predictions.[23,33–34] In this sense, it seems that for the systems under investigation, the low Reynolds number approach gives better results than the two-layer approach used in the enhanced wall treatment used in the RSM, R k-ε and S k-ε models.

Conclusions

A CFD model for simulating immobilized photocatalytic reactors was developed and evaluated against experimental data. The evaluation of the CFD model was performed using several hydrodynamic models that incorporated different near-wall modeling approaches. The performance of the model was assessed in terms of its capability for predicting the photocatalytic degradation rate of BA, as a model compound.

Under the used experimental conditions, the photocatalytic degradation of BA followed pseudo first-order kinetics with respect to both BA concentration and UV irradiance. The obtained kinetic expression is specific to the composite sol-gel TiO_2 coating, initial BA concentration, and dissolved oxygen concentration used in this study. This rate expression is expected to be applicable to other reactors as long as these variables remain similar to those in this work.

The experimental results and CFD simulations showed that the BA degradation rate in the analyzed photoreactors was limited by the rate of mass transport in the system. Under these conditions, the performance of CFD model was strongly determined by the external mass transfer prediction capability of the hydrodynamic models used. The CFD model photocatalytic reactor performance predictions were accurate when the laminar flow model, for laminar flow conditions, and the AKN or RSM turbulence models, for transitional and turbulent flow conditions, were applied.

The integrated model provided detailed description of the local photoreactor performance and identified the areas where improvement can be made. The model can be applied to better understanding of the reactor behavior and design optimization.

Acknowledgments

The authors acknowledge the Natural Sciences and Engineering Research Council of Canada (NSERC) for financial support and Alain Desprez for assisting with experimental and analytical work. J. Esteban Durán also thanks the support received from Universidad de Costa Rica.

Notation

A = area of the irradiated window, m^2
C = molar concentration, mol m^{-3}
Da = Damköhler number
D_m = molecular diffusivity of species k in the mixture, $m^2\ s^{-1}$
D_t = eddy (or turbulent) diffusivity for species concentration, $m^2\ s^{-1}$
E = radiation irradiance, W m^{-2}
E_{ex} = external effectiveness factor
I = unit tensor
j^e = emission (source) term, W $m^{-3}\ sr^{-1}$
J_i = diffusive flux of species i, kg $s^{-1}\ m^{-2}$
k = first-order reaction rate constant, s^{-1}
k'' = first-order surface reaction rate constant, m s^{-1}
k_c = mass transfer coefficient, m s^{-1}

L = photon radiance, W m^{-2} sr^{-1}
l = lamp arc length, m
m_i = mass fraction of species i
m_i' = fluctuating mass fraction of species i
M_W = molar weight, kg kmol^{-1}
n = refractive index
$\hat{n}$ = unit vector normal to the surface
N = total number of species
p = phase function for the in-scattering of photons
P = pressure, Pa
Q = flow rate, m^3 s^{-1}
r = position vector, m
r'' = molar surface reaction rate, mol s^{-1} m^{-2}
R_i^S = surface rate of production/depletion of species i, kg s^{-1} m^{-2}
Re = Reynolds number
Re_y = wall-distance-based turbulent Reynolds number
s = propagation direction vector, m
s' = scattering direction vector, m
Sc_t = turbulent Schmidt number
t = time, s
T = absolute temperature of the medium, K
TI = turbulence intensity
u = fluctuating flow velocity, m s^{-1}
U = velocity, m s^{-1}
V = volume, m^3
W = power output of the lamp, W
X_S = reactant conversion per pass
y = normal distance from the lamp center, m
y^+ = nondimensional distance from the wall
z = path length, m

Greek letters

α = reaction rate constant, m3 W^{-1} s^{-1}
β = half angle subtended by the lamp at the sensor position, rad
θ = residence time, s
κ = absorption coefficient, m^{-1}
μ = molecular viscosity, m^2 s^{-1}
μ_t = turbulent viscosity, m^2 s^{-1}
ρ = density, kg m^{-3}
σ = scattering coefficient, m^{-1}
$\sigma_{S\text{-}B}$ = Stefan-Boltzmann constant, 5.672×10^{-8} W m^{-2} K^{-4}
τ = viscous stress tensor, N m^{-2}
Φ = quantum yield of potassium ferrioxalate at 254 nm, mol einstein^{-1}
Ω' = solid angle about the scattering direction vector $\vec{s}'$, sr

Subscripts

app = apparent
B = bulk fluid phase
BA = benzoic acid
eff = effective
Fe^{2+} = ferrous ion
R = reactor
S = catalyst surface
T = total amount of liquid solution

Literature Cited

1. Pasternak J. Agricultural pesticide residues in farm ditches of the Lower Fraser Valley, British Columbia, Canada. *J Environ Sci Heal B*. 2006;41:647–669.
2. Kolpin DW, Furlong ET, Meyer MT, Thurman E, Zaugg SD, Buxton LB. Pharmaceuticals, hormones, and other organic wastewater contaminants in U.S. streams, 1999–2000: a national reconnaissance. *Environ Sci Technol*. 2002;36:1202–1211.
3. Ternes T. Occurrence of drugs in German sewage treatment plants and rivers. *Water Res*. 1998;32:3245–3260.
4. Herrmann J. Heterogeneous photocatalysis: state of the art and present applications. *Top Catal*. 2005;34:49–65.
5. Ollis DF, Pelizzetti E, Serpone N. Photocatalyzed destruction of water contaminants. *Environ Sci Technol*. 1991;25:1522–1529.
6. Li Puma G, Yue PL. A laminar falling film slurry photocatalytic reactor. Part I—model development. *Chem Eng Sci*. 1998;53:2993–3006.
7. Adesina AA. Industrial exploitation of photocatalysis: progress, perspectives and prospects. *Catal Surv Asia*. 2004;8:265–273.
8. Mukherjee PS, Ray AK. Major challenges in the design of a large-scale photocatalytic reactor for water treatment. *Chem Eng Technol*. 1999;22:253–260.
9. Kuipers JA, van Swaaij WP. Computational fluid dynamics applied to chemical reaction engineering. *Adv Chem Eng*. 1998;24:227–328.
10. Ranade V. *Computational Flow Modeling for Chemical Reaction Engineering*. London: Academic Press, 2002.
11. Mohseni M, Taghipour F. Experimental and CFD analysis of photocatalytic gas phase vinyl chloride (VC) oxidation. *Chem Eng Sci*. 2004;59:1601–1609.
12. Taghipour F, Mohseni M. CFD simulation of UV photocatalytic reactors for air treatment. *AIChE J*. 2005;51:3039–3047.
13. Salvado-Estivill I, Hargreaves DM, Li Puma G. Evaluation of the intrinsic photocatalytic oxidation kinetics of indoor air pollutants. *Environ Sci Technol*. 2007;41:2028–2035.
14. Jarandehei A, Visscher AD. Three-dimensional CFD model for a flat plate photocatalytic reactor: degradation of TCE in a serpentine flow field. *AIChE J*. 2009;55:312–320.
15. Romero-Vargas Castrillón S, de Lasa HI. Performance evaluation of photocatalytic reactors for air purification using computational fluid dynamics (CFD). *Ind Eng Chem Res*. 2007;46:5867–5880.
16. Pareek VK, Cox SJ, Brungs MP, Young B, Adesina AA. Computational fluid dynamic (CFD) simulation of a pilot-scale annular bubble column photocatalytic reactor. *Chem Eng Sci*. 2003;58:859–865.
17. Sengupta T, Kabir M, Ray A. A Taylor vortex photocatalytic reactor for water purification. *Ind Eng Chem Res*. 2001;40:5268–5281.
18. Denny F, Scott J, Pareek V, Peng G, Amal R. CFD modelling for a TiO_2-coated glass-bead photoreactor irradiated by optical fibres: Photocatalytic degradation of oxalic acid. *Chem Eng Sci*. 2009;64:1695–1706.
19. Periyathamby U, Ray AK. Computer simulation of a novel photocatalytic reactor using distributive computing environment. *Chem Eng Technol*. 1999;22:881–888.
20. Ray A. A new photocatalytic reactor for destruction of toxic water pollutants by advanced oxidation process. *Catal Today*. 1998;44: 357–368.
21. Duran JE, Taguipour F, Mohseni M. Evaluation of model parameters for simulating TiO_2 coated UV reactors. *Water Sci Technol.: Water Supply*. In press.
22. Sozzi DA, Taghipour F. Computational and experimental study of annular photo-reactor hydrodynamics. *Int J Heat Fluid Flow*. 2006;27:1043–1053.
23. Duran JE, Taghipour F, Mohseni M. CFD modeling of mass transfer in annular reactors. *Int J Heat Mass Transfer*. 2009 52, 5390–5401.
24. Duran JE, Mohseni M, Taghipour F. Modeling of annular reactors with surface reaction using computational fluid dynamics (CFD). *Chem Eng Sci*. 2010;65:1201–1211.
25. Duran JE, Taghipour F, Mohseni M. Irradiance modeling in annular photoreactors using the finite-volume method. *J Photochem Photobiol A*. 2010;215:81–89. doi:10.1016/j.jphotochem.2010.07.027.
26. Nallasamy M. Turbulence models and their applications to the prediction of internal flows: a review. *Comput Fluids*. 1987;15:151–194.
27. Wilcox D. *Turbulence modeling for CFD*. La Cañada, CA: DCW Industries, 2006.
28. Launder B, Spalding D. The numerical computation of turbulent flows. *Comput Method Appl M Eng*. 1974;3:269–289.
29. Shih T, Liou W, Shabbir A, Yang Z, Zhu J. A new k-ε eddy viscosity model for high Reynolds number turbulent flows—model development and validation. *Comput Fluids*. 1995;24:227–238.
30. Launder B, Reece G, Rodi W. Progress in the development of a Reynolds-Stress turbulence closure. *J Fluid Mech*. 1975;68:537–566.
31. Abe K, Kondoh T, Nagano Y. A new turbulence model for predicting fluid flow and heat transfer in separating and reattaching flows-I. Flow field calculations. *Int J Heat Mass Transfer*. 1994;37:139–151.
32. Fluent-Inc. *FLUENT 6.3 User's Guide. Chapter 12. Modeling Turbulence*. Lebanon, NH: Fluent-Inc., 2006.
33. Wang S, Mujumdar A. A comparative study of five low Reynolds number k-ε models for impingement heat transfer. *Appl Therm Eng*. 2005;25:31–44.
34. Wang Y, Postlethwaite J, Bergstrom D. Modelling mass transfer entrance lengths in turbulent pipe-flow with applications to small cathodes for measuring local mass transfer rates. *J Appl Electrochem*. 1996;26:471–479.

35. Spalding D. Concentration fluctuations in a round turbulent free jet. *Chem Eng Sci*. 1971;26:95–107.
36. Yimer I, Campbel I, Jiang L-Y. Estimation of the turbulent Schmidt number from experimental profiles of axial velocity and concentration for high-Reynolds-number jet flows. *Can Aeronaut Space J*. 2002;48:195–200.
37. Cassano AE, Martin CA, Brandi RJ, Alfano OM. Photoreactor analysis and design: fundamentals and applications. *Ind Eng Chem Res*. 1995;34:2155–2201.
38. Fluent-Inc. *FLUENT 6.3 User's Guide. Chapter 13.3. Modeling Radiation*. Lebanon, NH: Fluent-Inc., 2006.
39. Herz R. Intrinsic kinetics of first-order reactions in photocatalytic membranes and layers. *Chem Eng J*. 2004;99:237–245.
40. Edwards M, Villa C, Hill CG, Chapman T. Effectiveness factors for photocatalytic reactions occurring in planar membranes. *Ind Eng Chem Res*. 1996;35:712–720.
41. Camera-Roda G, Santarelli F. Optimization of the thickness of a photocatalytic film on the basis of the effectiveness factor. *Catal Today*. 2007;129:161–168.
42. Lide, D. *CRC Handbook of Chemistry and Physics* (89th edition). Boca Raton: CRC, 2008.
43. Thormählen I, Straub J, Grigull U. Refractive index of water and its dependence on wavelength, temperature and density. *J Phys Chem Ref Data*. 1985;14:933–945.
44. Noulty R, Lealst D. Diffusion coefficient of aqueous benzoic acid at 25°C. *J Chem Eng Data*. 1987;32:418–420.
45. Momentive. Available at: http://www.gequartz.com/en/optical.htm. Retrieved August 22, 2009.
46. Imoberdorf G, Taghipour F, Mohseni M. Radiation field modeling of multi-lamp, homogeneous photoreactors. *J Photochem Photobiol A*. 2008;198:169–178.
47. Pareek V, Adesina AA. Light intensity distribution in a photocatalytic reactor using finite volume. *AIChE J*. 2004;50:1273–1288.
48. Raithby G. Evaluation of discretization errors in finite-volume radiant heat transfer predictions. *Numer Heat Trans B: Fund*. 1999;36:241–264.
49. Keshmiri M, Mohseni M, Troczynski T. Development of novel TiO_2 sol-gel-derived composite and its photocatalytic activities for trichloroethylene oxidation. *Appl Catal B: Environ*. 2004;53:209–219.
50. Murov S, Carmichael I, Hug G. *Handbook of Photochemistry*. 2nd ed. New York: Marcel Dekker, Inc., 1993.
51. Romero R, Alfano O, Cassano A. Radiation field in an annular, slurry photocatalytic reactor. 2. Model and experiments. *Ind Eng Chem Res*. 2003;42:2479–2488.
52. Rahn R, Stefan M, Bolton J, Goren E, Shaw P, Lykke K. Quantum yield of the iodide-iodate chemical actinometer: dependence on wavelength and concentration. *Photochem Photobiol*. 2003;78:146–152.
53. Goldstein S, Rabani J. The ferrioxalate and iodide-iodate actinometers in the UV region. *J Photochem Photobiol A*. 2008;193:50–55.
54. Lawal O, Dussert B, Howarth C, Platzer K, Sasges M, Muller J, Whitby E, Stowe R, Adam V, Witham D, Engel S, Posy P, van de Pol A. Proposed method for measurement of the output of monochromatic (254 nm) low pressure UV lamps. *IUVA News*. 2008;10:14–17.
55. Fogler HS. *Elements of Chemical Reaction Engineering*. 4th ed. Upper Saddle River, NJ: Prentice Hall, 2006.
56. Hoffmann MR, Martin ST, Choi W, Bahnemannt DW. Environmental applications of semiconductor photocatalysis. *Chem Rev*. 1995;95:69–96.
57. Zhou S, Ray A. Kinetic studies for photocatalytic degradation of eosin B on a thin film of titanium dioxide. *Ind Eng Chem Res*. 2003;42:6020–6033.
58. Brosillon S, Lhomme L, Vallet C, Bouzaza A, Wolbert D. Gas phase photocatalysis and liquid phase photocatalysis: Interdependence and influence of substrate concentration and photon flow on degradation reaction kinetics. *Appl Catal B Environ*. 2008;78:232–241.
59. Mehrotra K, Yablonsky GS, Ray AK. Macro kinetic studies for photocatalytic degradation of benzoic acid in immobilized systems. *Chemosphere*. 2005;60:1427–1436.
60. Chen D, Li F, Ray A. Effect of mass transfer and catalyst layer thickness on photocatalytic reaction. *AIChE J*. 2000;46:1034–1045.
61. Dekker F, Bliek A, Kapteijn F, Moulijn J. Analysis of mass and heat transfer in transient experiments over heterogeneous catalysts. *Chem Eng Sci*. 1995;50:3573–3580.

Manuscript received Feb. 16, 2010, and revision received July 26, 2010.